Cavity-enhanced detection of spin polarization in a microfabricated atomic vapor cell

María Hernández Ruiz,[1,*] Yintao Ma,[1,2] Hana Medhat,[1] Chiara Mazzinghi,[1,3] Vito Giovanni Lucivero,[1,4] and Morgan W. Mitchell[1,5,†]

[1] *ICFO - Institut de Ciències Fotòniques, The Barcelona Institute of Science and Technology, Castelldefels (Barcelona) 08860, Spain*

[2] *School of Mechanical Engineering, Xi'an Jiaotong University, Xi'an 710049, China*

[3] *CNR-INO, Istituto Nazionale di Ottica, Sesto Fiorentino 50019, Italy*

[4] *Dipartimento Interateneo di Fisica, Universitá degli Studi di Bari Aldo Moro, Bari 70126, Italy*

[5] *ICREA - Institució Catalana de Recerca i Estudis Avançats, Barcelona 08010, Spain*

(Received 20 December 2023; revised 1 March 2024; accepted 13 May 2024; published 6 June 2024)

We demonstrate continuous Pound-Drever-Hall (PDH) nondestructive monitoring of the electron spin polarization of an atomic vapor in a microfabricated vapor cell within an optical resonator. The two-chamber silicon and glass cell contains ^{87}Rb and 1.3 amg of N_2 buffer gas, and is placed within a planar optical resonator formed by two mirrors with dichroic dielectric coatings to resonantly enhance the coupling to phase-modulated probe light near the D_2 line at 780 nm. We describe the theory of signal generation in this system, including the spin-dependent complex refractive index, cavity optical transfer functions, and PDH signal response to spin polarization. We observe cavity transmission and PDH signals across approximately 200 GHz of detuning around the atomic resonance line. By resonant optical pumping on the 795-nm D_1 line, we observe spin-dependent cavity line shifts, in good agreement with theory. We use the saturation of the line shift versus optical pumping power to calibrate the number density and efficiency of the optical pumping. In the unresolved sideband regime, we observe quantum noise limited PDH readout of the spin polarization density, with a flat noise floor of 9×10^9 spins cm^{-3} Hz$^{-1/2}$ for frequencies above 700 Hz. We note possible extensions of the technique.

DOI: 10.1103/PhysRevApplied.21.064014

I. INTRODUCTION

Sensing and metrology instruments based on optical pumping and atomic vapor spin physics [1,2], including atomic clocks [3] and sensors such as magnetometers [4], gyroscopes [5,6], and systems to test fundamental physics [7], offer high stability and sensitivity referenced to universally reproducible atomic spectral features. Many such instruments employ alkali metal atoms such as rubidium or cesium, in combination with methods such as buffer gas [8] or antirelaxation coatings [9] to reduce the depolarizing effects of wall collisions. Miniaturized vapor cells made with silicon microelectromechanical systems (MEMS) techniques [10–12] or with femtosecond laser writing [13] enable the miniaturization of such devices [14–18], while preserving the long coherence times and high atomic number densities that underlie their excellent performance.

Optical readout of vapor-based instruments complements optical pumping for spin control, and the quality of this readout has important effects on both sensitivity [19,20] and systematic effects [21]. With macroscopic cells, multipass geometries [22–25] have been used to enhance the effective length of the atomic medium, with a corresponding improvement in the ratio of information-carrying forward scattering to spin-randomizing side scattering [26]. Reduced dimensions limit the feasibility of this approach with MEMS cells.

An alternative to multipass methods, suitable for atomic volumes down to the wavelength scale [27], is the use of resonant structures, generically called "cavities." Like multipass methods, these maintain the probe photons in contact with the atomic medium longer than is possible in single-pass configurations. They moreover take advantage of the Purcell effect [28] of cavity quantum electrodynamics, which reduces side scattering and thus depolarization of the atomic medium. Resonant cavities have been used in precision measurement of atomic properties, for example for nondestructive readout of atomic population in atomic clocks [29,30], and for quantum

*Corresponding author: Maria.Hernandez@icfo.eu
†Corresponding author: morgan.mitchell@icfo.eu

 © 2024 American Physical Society

nondemolition measurement of cold-atom spin states using heterodyne [31] or homodyne [32,33] detection of the phase of the reflected light. Optical resonators have been used to enhance Faraday rotation in unpolarized [34] and polarized [35–37] spin ensembles. Approaches include both resonant, dichroism-based [35,38] and nonresonant, birefringence-based [34,36] probing. Calculations of cavity-enhanced Faraday rotation in cavity transmission [34,39] predict enhancement of the rotation angle [39] and other figures of merit [34] for dichroism- [38] and birefringence-based [34,39] rotation.

The Pound-Drever-Hall (PDH) method of cavity locking [40–42] is widely used in time-frequency metrology, and is analogous to frequency modulation spectroscopy techniques [43] used for high-resolution spectroscopy. In PDH, illustrated in Fig. 1 in Sec. II, a continuous-wave laser is phase modulated to produce sidebands above and below the carrier frequency. Upon reflection from the cavity, the carrier and sidebands acquire different, detuning-dependent phases, which converts some of the phase modulation to amplitude modulation. The resulting modulated power is directly detected with a fast photodetector and demodulated to obtain an error signal that, near resonance, is linear in the detuning, as seen in Fig. 2 in Sec. IV. The PDH method can be shot-noise limited, requires only a single optical polarization, and requires optical access to the cavity from only one side, all of which are attractive features for sensor miniaturization. Signal generation in PDH is described in greater detail in Appendices C to E.

Using the PDH method with vapors presents challenges not encountered when using PDH for, e.g., laser stabilization to empty reference cavities. Vapors, especially those housed with buffer gas to slow diffusion, have multigigahertz optical linewidths. Together with high atomic number densities, of the order of 1×10^{13} or 1×10^{14} cm^{-3}, these imply a significant broadening of cavity spectral lines due to atomic absorption, even in miniaturized cells. This absorption is moreover a function of the spin state, as the atoms can be found in states that are relatively "dark" or "bright" for the probe polarization. While quantitative models for atomic vapor optical properties [44], optical cavities containing dispersive media [45], and PDH signal acquisition [42] are all well established, to date no work has brought these together.

Here we demonstrate continuous PDH readout of the atomic spin dynamics of a ^{87}Rb vapor housed in a MEMS cell. We use planar mirrors with dichroic coatings to resonate probe light detuned by about 100 GHz from the D_2 line at 780 nm, while transmitting copropagating pump

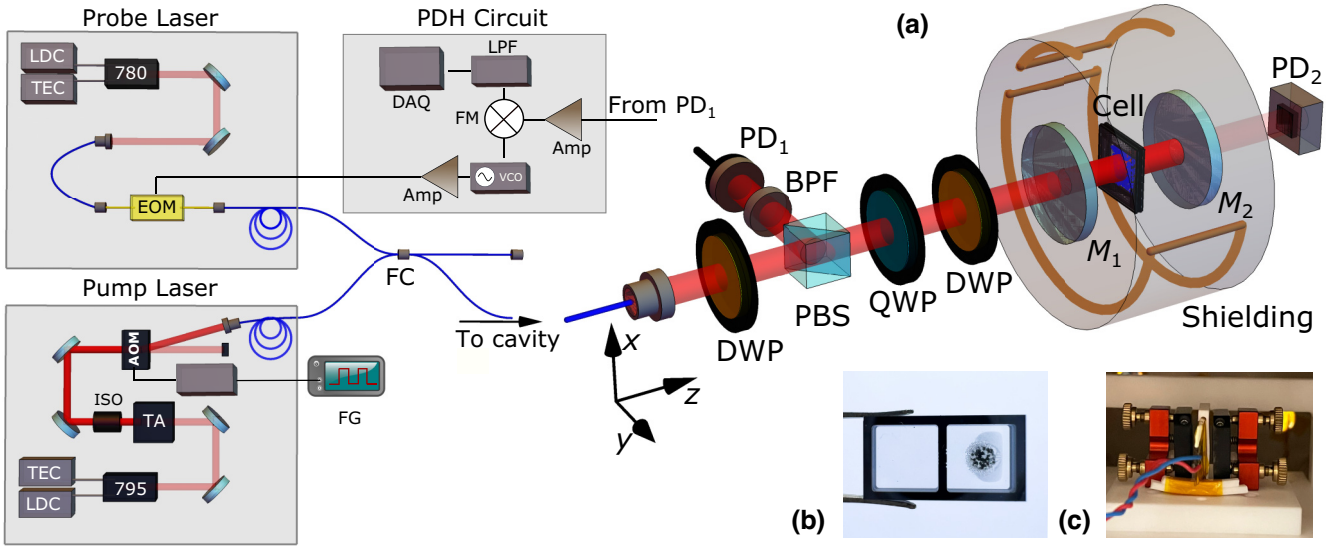

FIG. 1. Experimental setup for cavity-based detection of atomic polarization. Pump and probe beams are coupled into a fiber coupler (FC) and reach the atomic vapor within the cavity in the same collinear mode. The probe light is modulated in phase; the pump light is amplified and modulated in amplitude. The reflected probe is collected by a 125-MHz bandwidth photodetector PD_1, whose output is fed into a PDH circuit. A secondary detector PD_2 collects the transmitted light from the cavity. LDC, laser diode current controller; TEC, laser diode temperature controller; EOM, electro-optic modulator; TA, tapered amplifier; ISO, optical isolator; AOM, acousto-optic modulator; RFD, radio-frequency driver; FG, function generator; VCO, voltage-controlled oscillator; FM, frequency mixer; LPF, low-pass filter; DAQ, digital oscilloscope. (a) Sketch of the cavity with detection in reflection. DWP, dual wavelength wave plate; PBS, polarizing beam splitter; QWP, quarter-wave plate; BPF, laser line bandpass filter; PD, photodetector; M_1, first planar cavity mirror; M_2, second planar cavity mirror. (b) MEMS cell. Picture of the two-chamber microfabricated vapor cell after activation by UV decomposition of rubidium azide $^{87}RbN_3$. The physics (reservoir) chamber is in the left (right) portion of the cell. (c) Cavity and cell. Picture of the probe resonant cavity consisting of two planar mirrors surrounding the MEMS cell, which is heated and thermally insulated.

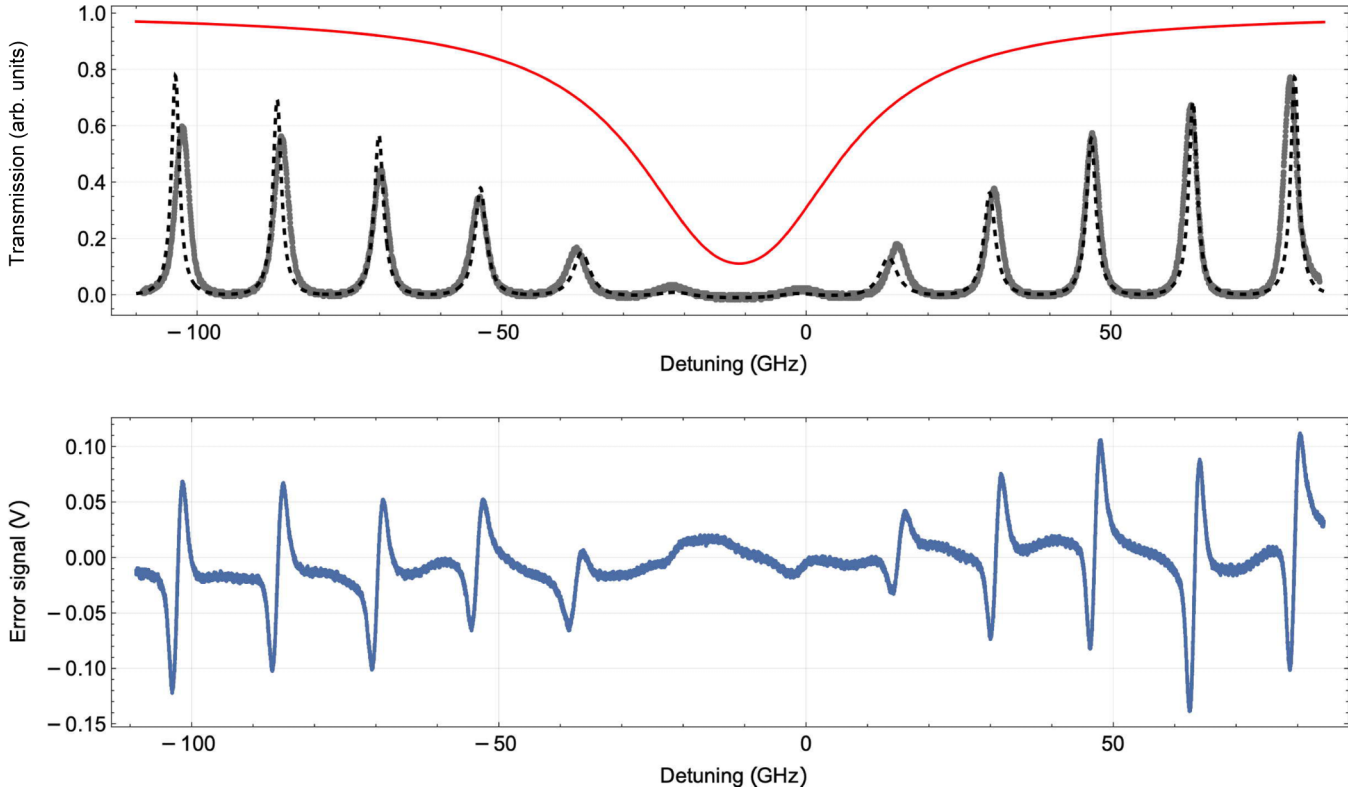

FIG. 2. Cavity transmission (top) and PDH error signal (bottom) near atomic resonance for a cavity containing a MEMS vapor cell. Detuning is measured with respect to the center of the D_2 transition of ^{87}Rb, and is positive for blue detuning. The red curve shows the calculated single-pass vapor intensity transmission $|t_A|^2$. Black and blue solid lines show the measured cavity transmission $|t_{cav}|^2$ and PDH error signal ϵ, respectively. Dashed black line shows fitting of the cavity transmission $|t_{cav}|^2$, with t_{cav} given by Eq. (C1) and the atomic medium single-pass transmission amplitude t_A given by Eq. (B2). For the fitting, the fixed parameters are the number density $n_A = 2.93 \times 10^{13}$ atoms/cm^3, the mirror reflectivities given in Sec. II, and the measured cell transmission amplitude $|t_{win}|^2 = 0.93$. Free parameters are the free spectral range $\Delta\nu_{FSR}$, the resonance shift Φ, and an overall scale factor.

light resonant with the D_1 line at 795 nm. We present a theoretical model that includes the complex refractive index of optically pumped, collisionally shifted and broadened atomic vapor, cavity transmission and reflection in the presence of the resulting circular birefringence and circular dichroism, and PDH signal generation in such a cavity. The theoretical model is applicable to both the slow-modulation or "unresolved sideband" regime and the fast-modulation or "resolved sideband" regime. Our experiment is limited to low cavity finesse due to atomic absorption and cell losses, which practically restricts us to the unresolved sideband regime. We find excellent agreement of the model with experimental observations in this regime.

The article is organized as follows. Section II presents the experimental system. Section III describes a model encompassing the cavity resonance shifts due to spin polarization (Sec. III A) and the resulting PDH error signal (Sec. III B). Section IV illustrates the experimental acquisition of PDH signals and demonstrates spin-dependent cavity line shifts. Section V calibrates the atomic response to optical pumping. Section VI shows experimental modulation of the spin polarization using amplitude-modulated optical pumping and the resulting raw photocurrent signal, including quantum noise limited spin detection. Section VII characterizes the demodulated signals and the observed sensitivity to spin polarization density. Section VIII compares the PDH method with other methods. Section IX describes possible extensions of the technique to improve sensitivity.

II. EXPERIMENTAL SYSTEM

The experimental setup is illustrated in Fig. 1. In the PDH probing scenario an electro-optic modulator (EOM) applies phase modulation at angular frequency Ω to a continuous-wave probe laser of angular frequency ω_0, chosen to be off resonance with respect to an atomic transition of interest. The resulting beam is circularly polarized and mode matched to a cavity containing an atomic medium. For this circular polarization, the refractive index and thus the cavity resonance frequency ω_{res} are functions of S_z, the on-axis component of the mean electron spin polarization. For simplicity, here and below

we assume that collisional broadening of the optical transition dominates over Doppler broadening and hyperfine splittings. In this scenario, (1) the spin variable that determines the refractive index will be the electron spin **S** and (2) the transition lineshape can be approximated as a Lorentzian. In scenarios for which collisional broadening does not dominate, the optical properties may be different. Upon reflection, the carrier and sidebands acquire phase shifts that depend on their respective detunings from cavity resonance, converting optical phase modulation into a detuning-dependent, and thus S_z-dependent, amplitude modulation. The reflected beam is collected with a 125-MHz bandwidth photodetector and the photocurrent is demodulated at frequency Ω with phase φ to obtain the quadrature amplitude ϵ, referred to as the PDH error signal. For laser-cavity detunings smaller than the cavity linewidth Γ, i.e. $|\omega_0 - \omega_{\rm res}| < \Gamma$, ϵ is approximately linear in $\omega_0 - \omega_{\rm res}$ and thus in S_z. In our specific implementation two collinear lasers are used to pump and probe the atoms. The pump laser is resonant with the ^{87}Rb D_1 line, whereas the probe laser is detuned from the D_2 line by angular frequency Δ. A MEMS vapor cell contains isotopically enriched ^{87}Rb vapor and 1.3 amg of N_2 due to prior UV decomposition of rubidium azide [10]. The MEMS cell consists of a silicon wafer, etched to create two $4 \times 4\,\text{mm}^2$ chambers joined by "microstrainer" conduits that allow gas and vapor diffusion between the chambers. Two 200-μm-thick Borofloat windows, attached by anodic bonding, seal the MEMS cell. The Si wafer thickness, and hence the experimental atomic interaction length, is $L_{\rm at} = 1.5\,\text{mm}$. The vapor cell is placed between two half-inch planar mirrors, whose cell-facing surfaces are coated to give reflectivities $R_1^{D_2} = 98.5\,\%$ and $R_2^{D_2} = 99\,\%$ for the probe light (near the 780-nm D_2 line) and transmissivities $T_1^{D_1} = T_2^{D_1} \approx 50\%$ for the pump light (at the 795-nm D_1 line), where $R_i = |r_i|^2$ and $T_i = 1 - R_i$, $i \in \{1, 2\}$, with the r_i reflection amplitude coefficients. The mirrors are mounted on high-stability nonmagnetic mounts, giving a free space cavity length of about $L_{\rm cav} = 9.2$ mm. The cell is heated by alternating-current Joule heating to a temperature of 126.5 ∘C, to achieve a number density of $n_A \approx 2.93 \times 10^{13}$ atoms/cm^3. The system comprising the cavity, the MEMS cell, and the oven is placed within one layer of μ-metal magnetic shielding. To implement the described PDH detection scheme, the output of an unmodulated distributed Bragg reflector (DBR) probe laser is phase modulated at $\Omega = 2\pi \times 114\,\text{MHz}$ using a fiberized electro-optical modulator (NIR-MPX800-LN-05) driven by an amplified voltage-controlled oscillator. Pump light is provided by a second DBR laser diode amplified by a tapered amplifier, which can generate up to 2 W of continuous-wave power at 795 nm. This output is passed through an acousto-optic modulator (AOM), whose first-order diffraction output is coupled into fiber. Switching off the AOM radio-frequency drive is used to block or unblock the pump beam. A 1×2 single-mode fiber coupler centered at 780 nm with ±15-nm bandwidth (Thorlabs PFC780A) combines orthogonally polarized pump and probe light into a single spatial mode, which is collimated and aligned with the cavity. As measured by a beam profiler, the beam appears Gaussian, with beam diameters ($1/e^2$ of intensity) of 1.16 and 0.91 mm in the x and y directions, respectively. As shown in Fig. 1, a dual wavelength wave plate (DWP) rotates the probe polarization such that both collinear beams are horizontally polarized along the y direction to give maximum transmission through a polarizing beam splitter (PBS). A zero-order quarter-wave plate (QWP) converts both to circular polarization. A second DWP can be inserted to control the direction of the pump beam circular polarization without changing the probe's circular polarization. Probe light reflected from the cavity is directed by the same PBS to a 125-MHz bandwidth photodetector PD $_1$, whose output current is demodulated by the PDH circuit to provide the error signal, which is digitized by a data acquisition card, as illustrated in Fig. 1. The reflected pump light is filtered out at the detection stage by a bandpass filter centered at 780 nm with 3-nm bandwidth and an optical density of 6 at 795 nm.

III. PDH SPIN MEASUREMENT

We now describe the cavity response to an optically induced polarization. The optical response of the atomic vapor and the structure of the cavity resonances that determine the PDH signal are described in Appendices A to E.

A. Cavity resonance shifts due to atomic spin polarization

As derived in Appendix D, the shift in the cavity resonance frequency due to polarization is given by

$$\delta\nu = \frac{\pm\mathcal{D}_0 c\tilde{\alpha}^{(1)}}{4\pi L_{\rm cav}} \frac{\nu}{\nu_{\rm at}} \frac{(\Delta\nu_{\rm opt}^{D_2}/2)(\nu - \nu_{\rm at})}{(\nu - \nu_{\rm at})^2 + (\Delta\nu_{\rm opt}^{D_2}/2)^2} P_z, \qquad (1)$$

where $\mathcal{D}_0$ is the on-resonance optical depth of the unpolarized medium [Eq. (B3)], c is the speed of light, $\tilde{\alpha}^{(1)} = -2$ for the D_1 transition or $\tilde{\alpha}^{(1)} = 1$ for the D_2 transition, ν is the resonance linear frequency, $\nu_{\rm at}$ and $\Delta\nu_{\rm opt}^{D_2}$ are respectively the line center and FWHM of the atomic absorption resonance (linear frequency), and we have defined the degree of polarization $P_z \equiv 2S_z$ equal to 1 for maximum spin polarization [47,48].

B. PDH error signal

As described in Appendix E, the PDH signal after demodulation is

$$\epsilon = K \sum_{k=-\infty}^{\infty} J_k(\beta) J_{k+1}(\beta) 2\text{Re}[r_{\rm cav}^*(\omega_k) r_{\rm cav}(\omega_{k+1}) e^{i\varphi}], \qquad (2)$$

where K is the overall gain of the system, including the laser power, photodetector responsivity, and the gains of the amplification and demodulation subsystems; $J_k(\beta)$ is the Bessel function of the first kind of order k; β is the phase modulation amplitude; $r_{\rm cav}$ is the frequency-dependent cavity reflection amplitude given in Eq. (C3); $\omega_k \equiv \omega_0 + k\Omega$, where ω_0 is the probe carrier frequency; Ω is the modulation frequency; and φ is the demodulation phase.

IV. PDH SIGNAL CHARACTERIZATION

For wide frequency scans over 200 GHz, as in Fig. 2, we control the laser output frequency via the laser diode temperature. The frequency-temperature relation is monotonic but nonlinear, so for wide frequency scans, as in Fig. 2, we use a fiber Mach-Zehnder interferometer with a 41.28-MHz repeat period [49] to calibrate the frequency scale. We use as an absolute frequency reference either a wavemeter or the transmission of a spectroscopy cell containing ^{87}Rb in vacuum.

The simultaneously acquired transmission and PDH reflection signals are shown in Fig. 2. Also shown is a fit of Eq. (C1) to the transmission signal, which shows good agreement for the spectral positions and widths of the transmission peaks. In both the experiment and the model, the heights of the transmission peaks are greatly reduced near atomic resonance, due to intracavity absorption. The heights of the experimentally observed peaks show an asymmetry that is not present in the model. We attribute this to etalon effects produced by weak reflections from the cell windows, which are not included in the model.

Focusing on a single resonance detuned by about 115 GHz, the left panel of Fig. 3 shows representative PDH error signals $\epsilon(\nu)$ for unpolarized atoms and for polarized atoms pumped with $\sigma_\pm$ circularly polarized light. The chosen detuning of approximately 115 GHz reflects the tradeoff between finesse, which is larger for larger detuning due to reduced atomic absorption, and spin dependence of the resonant frequency, which is larger for smaller detuning. To acquire these spectra, we apply a 500-Hz triangle-wave modulation to the probe laser current, to scan the probe carrier frequency, while applying phase modulation as described in Sec. II. We synchronously apply a 250-Hz square-wave modulation to the rf driver of the AOM, so that the pump power is "off" for one scan of the resonance, and then "on" for the next. Combination and rotation of the QWP and DWP are used to switch between σ_+ and σ_- polarizations of the pump beam.

Optical pumping induces a nonzero S_z and thus modifies the refractive index n, both real and imaginary parts. Change in the real part n' causes a shift of the resonance frequency, given by Eq. (D4), and a corresponding frequency shift of the error signal feature. Change of the imaginary part n'' alters the finesse of the resonance, and thus the peak-to-peak amplitude of the error signal. Both

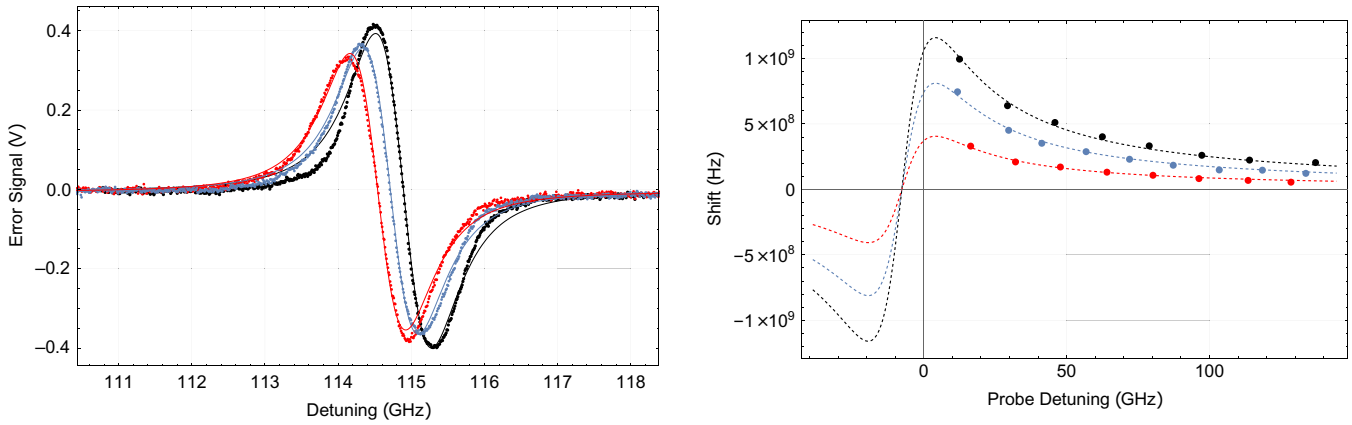

FIG. 3. Response of the PDH signal to optical pumping. Left: PDH error signal ϵ, obtained with modulation frequency $\Omega = 2\pi \times 114$ MHz and strong modulation depth $\beta = 1.78$, in scans around a single cavity resonance. Detuning is measured with respect to the line center of the atomic resonance of transition D_2 of ^{87}Rb. The probe light is σ_- polarized and detuned to the blue side of the atomic resonance. Blue dots show ϵ acquired with no optical pumping; red and black dots show ϵ acquired with σ_- and σ_+ optical pumping, respectively. The pump power is $P_{\rm pump} = 22$ mW, which induces a degree of polarization of $P_z = 0.65$ [calculated using Eq. (D4)]. Continuous lines in the same colors show fits to the data with Eq. (2), with the resonance line center ν_p for polarization $p \in \{0, \sigma_\pm\}$, finesse $\mathcal{F}$, and system gain K as free parameters. Line shift due to σ_+ pumping is calculated as $\delta\nu_{\rm shift} = \nu_{\sigma_+} - \nu_0$. Right: line shift versus detuning from atomic resonance $\Delta/2\pi$ for different degrees of polarization. Red, blue, and black points show $\delta\nu_{\rm shift}$ acquired by fitting scans, as just described, for optical pumping powers of 5, 15, and 55 mW, respectively. Each dot shows the average $\delta\nu_{\rm shift}$ of 20 pairs of fits. Dashed lines show fits of Eq. (D4) to the measured shifts, and yield $P_z = 0.29$, 0.57, and 0.82 (from bottom to top). In these fits P_z is the sole free parameter; fixed parameters are $L_{\rm at} = 1.5$ mm (manufacturer's specification), $L_{\rm cav} = 9.2$ mm (from measured $\Delta\nu_{\rm FSR}$), $\Delta\nu_{\rm opt}^{D_2} = 23.5\,{\rm GHz} = 18.1\eta$ [46] (with measured N_2 density $\eta = 1.3$ amg), and $n_A = 2.93 \times 10^{13}$ atoms/cm^3.

effects are clearly observed in Fig. 3. The error signals are fitted by using Eq. (2) (details in the caption of Fig. 3).

The right panel of Fig. 3 shows the shift $\delta\nu_{\rm res}$ of the resonance frequency due to optical pumping, defined as the change in the zero crossing of ϵ when pumped with σ_+ light, relative to the zero crossing when unpumped. To measure this for a given probe detuning Δ and pump power $P_{\rm pump}$, we acquire 20 scans with pumping and 20 scans without pumping, fit them as described above, and compute the mean shift. We acquired three different $P_{\rm pump}$ levels, each at different values of Δ. In order to get the different degrees of polarization for each $P_{\rm pump}$ level, we fit the data with Eq. (D4), the theoretical shift in resonance frequency, with only P_z as the free parameter.

V. OPTICAL PUMPING AND ATOM NUMBER DENSITY CALIBRATION

We describe the optical physics with a "plane-wave" model of the optical pumping and cavity response. That is, we ignore the variation of optical intensity and resulting polarization with transverse position within the pump and probe beams. Optical pumping with σ_+ light, in competition with linear relaxation processes, produces an equilibrium spin polarization [47]

$$S_z = \frac{a_{\rm OP} R_{\rm OP}}{2a_{\rm OP}R_{\rm OP} + R_{\rm rel}}, \tag{3}$$

where $a_{\rm OP}$ is the average angular momentum added per absorbed photon and $R_{\rm rel}$ is the spin relaxation rate. The rate of optical pumping is

$$\begin{aligned} R_{\rm OP} &= \sigma_{\rm abs}(\nu)\phi_{\rm phot} \\ &= r_e c f_{\rm osc}^{D_1} \frac{\Delta\nu_{\rm opt}^{D_1}/2}{(\nu_{\rm pump} - \nu_{\rm at}^{D_1})^2 + (\Delta\nu_{\rm opt}^{D_1}/2)^2} \frac{I_{\rm pump}}{\hbar\omega} \\ &\overset{\rm res}{=} \frac{r_e c f_{\rm osc}^{D_1}}{\Delta\nu_{\rm opt}^{D_1}/2} \frac{I_{\rm pump}}{\hbar\omega}, \end{aligned} \tag{4}$$

where $\sigma_{\rm abs}$ is the absorption cross section and $\phi_{\rm phot}$ is the photon flux density, $I_{\rm pump}$ is the pump intensity, and the third line of Eq. (4) holds for resonant pumping $\nu = \nu_{\rm at}^{D_1}$, a condition we indicate with the label "res".

It is convenient to write Eq. (3) as

$$S_z \overset{\rm res}{=} \frac{1}{2}\frac{I_{\rm pump}}{I_{\rm pump} + I_{\rm sat}}, \tag{5}$$

where the on-resonance saturation pump intensity is

$$I_{\rm sat} = \frac{\Delta\nu_{\rm opt}^{D_1}\hbar\omega}{a_{\rm OP} r_e c f_{\rm osc}^{D_1}} R_{\rm rel}. \tag{6}$$

For quantitative modeling of the optical pumping, the spatial distribution of S_z due to pump absorption [50] and a consequent integral over the cell length should be considered [51]. This description, however, is outside the scope of this current work. Instead, we adopt the heuristic model

$$S_z = \frac{1}{2}\frac{P_{\rm pump}}{P_{\rm pump} + P_{\rm sat}} \overset{\rm ssr}{\approx} \frac{1}{2}\frac{P_{\rm pump}}{P_{\rm sat}}, \tag{7}$$

where $P_{\rm sat}$ is the saturation pump power, and the approximation holds in the small-signal regime (ssr) $P_{\rm pump} \ll P_{\rm sat}$.

Using Eq. (D4), this implies that the resonance shift

$$\delta\nu = \delta\nu_{\rm max}(\nu_{\rm probe})\frac{P_{\rm pump}}{P_{\rm pump} + P_{\rm sat}}, \tag{8}$$

where, for $\sigma_\pm$ probe light,

$$\delta\nu_{\rm max}(\nu) = \frac{\pm\mathcal{D}_0 c g}{4\pi L_{\rm cav}} \frac{\nu}{\nu_{\rm at}} \frac{(\Delta\nu/2)(\nu - \nu_{\rm at})}{(\nu - \nu_{\rm at})^2 + (\Delta\nu/2)^2} \tag{9}$$

is the asymptotic frequency shift. Figure 4 shows fits of Eq. (8) to data (the same results as in the right panel of Fig. 3), yielding $P_{\rm sat} = 11.7\,{\rm mW}$ and $n_A = 2.93 \times 10^{13}$ atoms/cm^3 (in $\mathcal{D}_0$), with good agreement.

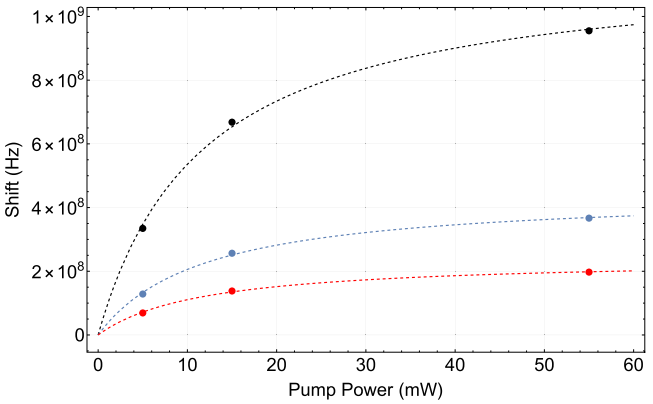

FIG. 4. Shift of the error signal $\delta\nu_{\rm shift}$ versus the pump power $P_{\rm opt}$ for probe detunings $\nu - \nu_{\rm at} = 15$ (black), 65 (blue), and 130 GHz (red). We take $\nu_{\rm at}$ to be the center of the D_2 transition of ^{87}Rb. Points show $\delta\nu_{\rm shift}$ obtained by fitting pumped and unpumped single-resonance error spectra, as in the left panel of Fig. 3. Curves show fits with Eq. (8), with $\delta\nu_{\rm max}(\nu)$ and $P_{\rm sat}$ as free parameters. The fits yield $P_{\rm sat} = 11.7\,{\rm mW}$, $\delta\nu_{\rm max}(15\,{\rm GHz}) = 1.16\,{\rm GHz}$, $\delta\nu_{\rm max}(65\,{\rm GHz}) = 0.47\,{\rm GHz}$, and $\delta\nu_{\rm max}(130\,{\rm GHz}) = 0.24\,{\rm GHz}$.

VI. MODULATION OF S_z AND RAW PHOTOSIGNAL

To study the response of the cavity to changes in spin polarization, we apply phase modulation to the probe as described in Sec. II. Because our photodetector is not shot-noise limited at the 114-MHz frequency used until now,

for the remaining measurements, we use a modulation frequency of 19 MHz. The signal from PD_1 (see Fig. 1) is split into dc and rf components with a bias tee. The rf component is amplified and further split with a 3-dB splitter, one output of which goes to a spectrum analyzer (SA), the other of which goes to the demodulation system (mixer and low-pass filter). Based on the demodulated signal, the probe carrier frequency ω_0 is manually set to the center of the resonance and during the acquisition remains within the central region, i.e., the region of negative slope in the left panel of Fig. 3. Representative spectra are shown in the left panels of Fig. 5.

We apply a sinusoidally modulated pump power

$$P_{\text{pump}} = P^{(0)}_{\text{pump}} + \tfrac{1}{2} P^{\text{P-P}}_{\text{pump}} \cos \Omega_{\text{pump}} t, \tag{10}$$

where $P^{\text{P-P}}_{\text{pump}}$ is the peak-to-peak variation of the pump power and $\Omega_{\text{pump}}/2\pi \approx 1\,\text{kHz}$ is the modulation frequency. This induces a sinusoidal shift in the PDH line center. This, in turn, produces a periodic modulation at frequency Ω_{pump} of the amplitude modulation at Ω seen by PD_1. This manifests as signal sidebands at $\Omega \pm \Omega_{\text{pump}}$, and distortion sidebands at $\Omega \pm j\,\Omega_{\text{pump}}$, $j = 2, 3, \ldots$. We study two signal regimes: with $P^{\text{P-P}}_{\text{pump}} = 1\,\text{mW}$ of resonant pump power, we access the small-signal regime, in which the root-mean-squared (rms) line shift $\delta\nu^{\text{rms}}_{\text{shift}} \ll \Gamma_{\text{cav}}$, and the distortion sidebands are nearly 20 dBm below the signal sidebands; with $P^{\text{P-P}}_{\text{pump}} = 30\,\text{mW}$, we access the large-signal regime, with $\delta\nu^{\text{rms}}_{\text{shift}} \sim \Gamma_{\text{cav}}/2$. With this $P^{\text{P-P}}_{\text{pump}}$, the distortion sidebands are about 10 dBm below the signal sidebands.

These spectra also show a strong peak at the probe phase modulation frequency $\Omega = 2\pi \times 19\,\text{MHz}$, which results from drift of ω_0 away from line center. Noise in the band $\Omega - 2\pi \times 700$ to $\Omega + 2\pi \times 700\,\text{Hz}$ is comparable to or weaker than the applied signal. The noise in this frequency band can be attributed to small and slow shifts in the probe laser frequency, e.g., those due to laser temperature changes.

Other frequency bands show a flat noise spectrum about 2 dB above the electronic noise level of the acquisition, obtained with $P_{\text{probe}} = 0$. We interpret this 2-dB contribution as quantum noise: the sum of photon shot noise and the broadband component of atomic spin projection noise [52]. We note that the noise background does not rise in going from the small-signal to large-signal regime. This indicates a negligible level of technical noise associated with the optical pumping of the spins and with the increased signal strength.

VII. DEMODULATED PDH SIGNAL AND SENSITIVITY

In the right panels of Fig. 5, we show spectra of the demodulated photocurrent, i.e., the PDH error signal ϵ, acquired under the same conditions as described in Sec. VI. As expected for the demodulation process, the spectrum strongly resembles that of the left panels of Fig. 5, downshifted by the modulation frequency Ω.

A narrow peak at 1 kHz is the signal, due to applied pump modulation. Noise in the band below approximately 700 Hz shows peaks at the 50-Hz mains frequency and harmonics. Outside this band, the noise is spectrally flat, and once again we interpret this as the combined photon shot noise and spin projection noise. Again, we note the near absence of detectable technical noise associated with optical pumping and a strong signal, with the possible exception of a small peak near 1.2 kHz.

We identify the sensitivity of the measurement, i.e., equivalent spin noise spectral density, as follows. Considering the trace taken in the small-signal regime, for which we can use Eq. (3) to convert from P_{pump} to S_z, we note that the applied monochromatic pump power modulation, with mean squared variation $(P^{\text{P-P}}_{\text{pump}})^2/8$, produces, by Eq. (7), a mean square variation in $n_{\text{A}} S_z$ of

$$\mathcal{P}_{n_{\text{A}} S_z} = \frac{n_A^2}{8} \left(\frac{P^{\text{P-P}}_{\text{pump}}}{2P_{\text{sat}}} \right)^2. \tag{11}$$

This single-frequency "signal-like" feature is represented in the SA's spectrum by a peak of height $P^{\text{ref}}_{\text{SA}} \equiv P_{\text{SA}}(\nu_{\text{pump}})$ with units of electrical power. The conversion from pump power to spin density signal power is thus $\mathcal{P}_{n_{\text{A}} S_z}/P^{\text{ref}}_{\text{SA}}$. Meanwhile, the broad "noiselike" features of the same spectrum must be interpreted as an electrical power spectral density $P_{\text{SA}}(\nu)/\Delta\nu^{\text{RBW}}$, or after conversion to spin units, the spin-noise power spectral density

$$\mathcal{S}_{n_{\text{A}} S_z}(\nu_{\text{sig}}) = \frac{P_{\text{SA}}(\nu_{\text{sig}})}{P^{\text{ref}}_{\text{SA}} \Delta\nu^{\text{RBW}}} \frac{n_A^2}{8} \left(\frac{P^{\text{P-P}}_{\text{pump}}}{2P_{\text{sat}}} \right)^2, \tag{12}$$

where all P quantities have units of electrical power [$P_{\text{SA}}(\nu_{\text{sig}})$ and $P^{\text{ref}}_{\text{SA}}$] or optical power ($P^{\text{P-P}}_{\text{pump}}$ and P_{sat}). Here $\mathcal{S}_{n_{\text{A}} S_z}(\nu_{\text{sig}})$ is a power spectral density with units of $\text{spins}^2/\text{cm}^6/\text{Hz}$. In the right panels of Fig. 5, we graph the square root of this quantity, the amplitude spectral density (ASD), with units of $\text{spins cm}^{-3}\,\text{Hz}^{-1/2}$. In analogy to the noise-equivalent power that describes detector sensitivity, $\mathcal{S}^{1/2}_{n_{\text{A}} S_z}(\nu_{\text{sig}})$ is the noise-equivalent spin density of the measurement.

VIII. COMPARISON TO OTHER METHODS

As described in Sec. I, a variety of optical enhancement methods, including multipass and cavity enhancement, have been used for sensing and metrology applications that require sensitive nondestructive measurement of atomic polarization. While it is clear that optical enhancement methods improve relevant figures of merit for these applications, e.g., magnetic sensitivity for magnetometers

[24,35], scattering for atomic state measurement [34], or short-term stability for atomic clocks [29], to our knowledge, there is no established figure of merit that allows comparison across applications. We can nonetheless note some commonalities. In multipass methods with fixed medium length, the signal, e.g., an accumulated phase or Faraday rotation angle, grows linearly with the number of passes. Similarly, in cavity enhancement, again with fixed cavity length and thus fixed free spectral range (FSR), the slope $d[\arg(r_{\rm cav})]/d\omega$ of the reflected phase is inversely proportional to the cavity linewidth, and thus proportional to the finesse. We can thus identify the number of passes and the finesse as roughly comparable measures for signal enhancement. The number of passes range from tens in magnetometry [24] to hundreds in trace-gas spectroscopy [53], while finesses range from about 10 in about 10 cm cavities containing vapor cells [34,35] to about 10^5 for cold-atom cavities in vacuum [32]. The finesse in this experiment depends on the intracavity atomic absorption and thus the detuning. For a detuning of $2\pi \times 115$ MHz as in Fig. 3, we have $\mathcal{F} \approx 18$, similar to values obtained with larger vapor cells.

IX. OUTLOOK

We note a few possible improvements. The current system operates in the unresolved sideband regime, with $\Omega \ll \Gamma$. In this regime, the signal strength is proportional to Ω. A better sensitivity can thus be expected simply by operating at higher Ω. To do so with shot-noise-limited performance would require a different detector, one that is shot-noise limited at similar power levels and higher frequencies. We note that using specific detector geometries, detectors with shot-noise-limited bandwidths of 9 GHz [54] have been demonstrated, with potential to reach still much higher frequencies [55].

Our system is implemented with a microfabricated vapor cell inside a cavity formed by independent mirrors. Losses on the cell windows limit the finesse of the resonant cavity in this geometry. A vapor cell in which the internal surfaces were coated would have a finesse limited in principle only by the reflectivity of the cavity mirrors, which would double as interior surfaces of the vapor cell. We note that ^{87}Rb MEMS cells with (nonoptical) internal coatings [10] have been demonstrated.

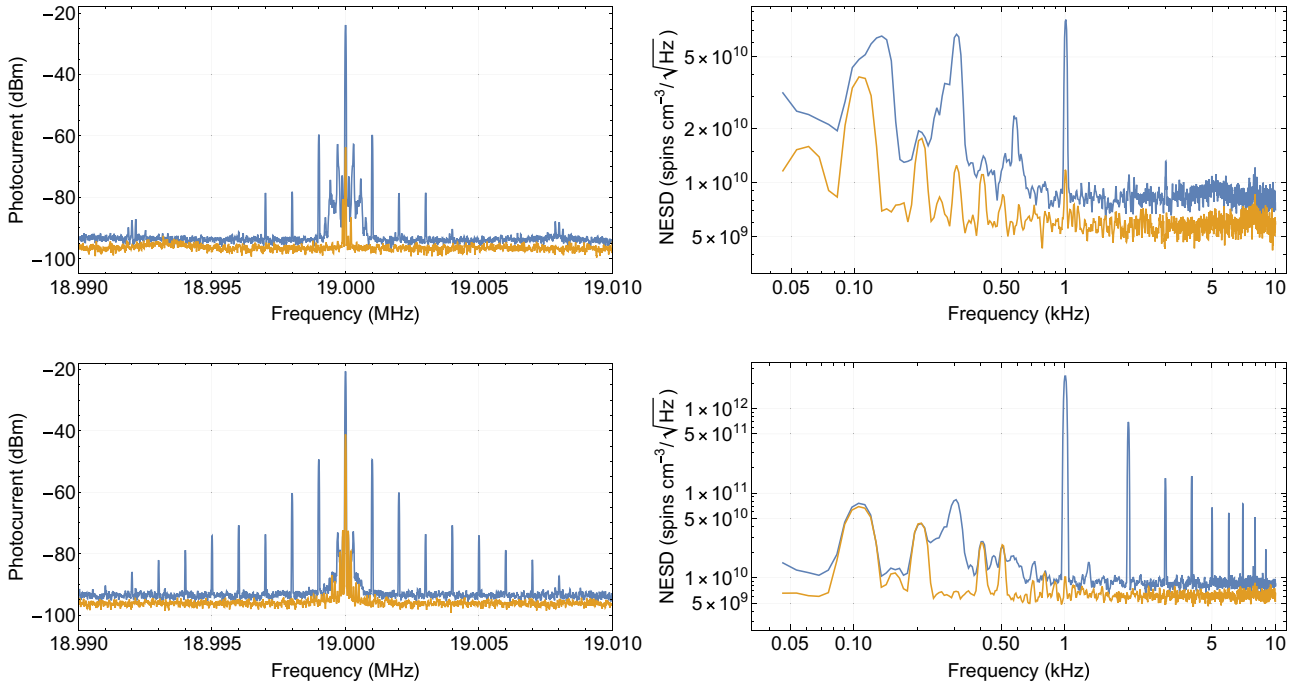

FIG. 5. Signal and noise in PDH detection of S_z modulation induced by optical pumping. Left graphs show spectrum analyzer traces of the detector photocurrent, expressed in electrical power units (decibels). Right graphs show the spin sensitivity of the PDH error signal, i.e., of the photocurrent after demodulation, expressed as the noise-equivalent spin density (NESD) with units of spins cm^{-3} Hz$^{-1/2}$ (see the text for details of the calibration). Upper graphs were acquired in the small-signal regime with an optical pumping power of 1-mW peak-to-peak sinusoidal modulation at 1 kHz. Lower graphs acquired in the large-signal regime with an optical pumping power of 30-mW peak-to-peak sinusoidal modulation at 1 kHz. Orange curves, acquired with zero probe laser power, show detection and demodulation electronic noise background. Blue curves, acquired with 2.8 mW of probe laser, detuned 120 (upper) or 100 GHz (lower) to the blue of the center of the unshifted D_2 resonance, and with σ_- polarization, include signal and optical noise. Spectra acquired with a digital spectrum analyzer with equal resolution bandwidth and video bandwidth $\Delta\nu^{\rm RBW} = 30$ Hz.

X. CONCLUSIONS

We have implemented optically resonated readout of the spin polarization of an atomic vapor in a microfabricated vapor cell. We use a planar cavity, resonant for the D_2 line of ^{87}Rb, and Pound-Drever-Hall detection of cavity line shifts produced on circularly polarized probe light, to detect the electron spin polarization S_z of a dense vapor ^{87}Rb in 1.3 amg of N_2 buffer gas. We present a model for the resulting signals, combining theory of the vector polarizability of alkali vapors, resonant cavity response, and Pound-Drever-Hall signal generation. We find good agreement of the model with experimental observations, and demonstrate a quantum noise limited sensitivity to spin density of approximately 9×10^9 spins cm^{-3} Hz$^{-1/2}$. The technique has potential to provide high-efficiency readout for miniaturized atomic vapor sensing and metrology instruments, in the same way that cavity-enhanced readout has been used with cold-atom instruments.

ACKNOWLEDGMENTS

We thank Jakob Reichel for insights about cavity enhancement; Kostas Mouloudakis, Michael Tayler, and Aleksandra Sierant for laboratory assistance and helpful discussions; and Jacques Haesler, Sylvain Karlen, and Thomas Overstolz of the Centre Suisse d'Electronique et de Microtechnique SA (CSEM) in Neuchâtel (Switzerland) for providing MEMS vapor cells. This work was supported by European Commission projects MACQSIMAL (820393), OPMMEG (101099379), and QUANTIFY (101135931); NextGenerationEU (PRTR-C17.I1); Spanish Ministry of Science (MCIN) project SAPONARIA (PID2021-123813NB-I00); "Severo Ochoa" Center of Excellence CEX2019-000910-S, Departament de Recerca i Universitats de la Generalitat de Catalunya Grant No. 2021 SGR 01453; Fundació Privada Cellex; and Fundació Mir-Puig. M.H.R. acknowledges support from Ayuda PRE2021-098880 financiada por MCIN/AEI/10.13039/501100011033 y por el FSE+. V.G.L. acknowledges financial support from European Union NextGenerationEU (PNRR MUR project PE0000023 – NQSTI) and from the Italian Ministry of University and Research (MUR) project "Budget MIUR - Dipartimenti di Eccellenza 2023 - 2027" (Law 232, 11 December 2016) - Quantum Sensing and Modelling for One-Health (QuaSiModO). H.M. acknowledges financial support from the European Union's Horizon Europe research and innovation programme under the Marie Sklodowska-Curie Grant Agreement No. 101081441. Y.M. acknowledges the support from China Scholarship Council (202206280171).

V.G.L. and M.W.M. jointly supervised this work.

APPENDIX A: ATOMIC VAPOR REFRACTIVE INDEX

For low-density media such as vapors, local-field effects can be neglected and the electric susceptibility calculated as $\chi = n_A \alpha$ [56], where n_A is the atomic number density and α is the atomic polarizability. In general, χ and α are complex-valued rank-two tensors, as required to describe circular dichroism and circular birefringence. Also, in these conditions the refractive index is given, in cgs units, by $n = \sqrt{1 + 4\pi n_A \alpha} \approx 1 + 2\pi n_A \alpha$ or

$$(n - 1) \approx 2\pi n_A \alpha. \tag{A1}$$

The following calculations concern the linear-optical susceptibility and polarizability, and assume that the optical transitions are not saturated by probe or pumping light. A general condition for the validity of this assumption is [56]

$$\Omega_{\text{opt}} \ll \frac{1 + \Delta^2 \Gamma_2^{-2}}{4\Gamma_1^{-1}\Gamma_2^{-1}}, \tag{A2}$$

where $\Omega_{\text{opt}} = |E d_{ba}|/\hbar$ is the optical Rabi frequency, with d_{ba} the optical transition electric dipole moment between ground state $|a\rangle$ and excited state $|b\rangle$, and Γ_1 is the corresponding longitudinal coherence relaxation rate. Equation (A2) holds in all the experimental conditions we present in this work.

The calculation of the atom's state-dependent electric polarizability tensor α is extensively discussed in the optical pumping literature; see, for example, Refs. [2,44,57]. The ac-Stark shift of the ground state, obtained by taking the electric dipole interaction in second order and by adiabatic elimination of the excited state, is given by [44, Eq. 6.73]

$$\delta H = -\mathbf{E} \cdot \alpha \cdot \mathbf{E}^*, \tag{A3}$$

where $\mathbf{E} = |\mathbf{E}|\mathbf{e}$ is the complex vector amplitude of the optical electric field. We work with quantization axis z, so the $\sigma_\pm$ and π polarizations are described by $\mathbf{e}_\pm \equiv (\hat{\mathbf{x}} \pm i\hat{\mathbf{y}})/\sqrt{2}$ and $\mathbf{e}_0 \equiv \hat{\mathbf{z}}$, respectively. Here α is in general a second-rank tensor, with irreducible scalar, vector ("gyrotropic"), and tensor ("birefringent") parts. For our experimental conditions, the collisional broadening is much larger than the excited-state hyperfine splitting and the Doppler broadening. Consequently, the optical transition can be treated as homogeneously broadened, and the tensor part of the susceptibility can be neglected, leaving only the scalar and vector parts. In these conditions, the susceptibility in Cartesian coordinates is [44, Eqs. 5.41,

6.73, 6.75]

$$\alpha_{ij} = \alpha_0\left(\frac{1}{2}\delta_{ij} + \frac{2(-1)^{J-1/2}}{[J]} i\epsilon_{ijk}S_k\right), \tag{A4}$$

where δ_{ij} is the Kronecker symbol and ϵ_{ijk} is the Levi-Civita symbol. Summation over repeated indexes is implied, and [44, Eq. 5.45]

$$\alpha_0 = \frac{r_e c^2 f_{\rm osc}}{\omega_{\rm at}} \frac{-1}{\Delta + i\Gamma_2}, \tag{A5}$$

where $f_{\rm osc}$ is the relevant oscillator strength. Within the planar resonator of the optical cavity, the optical field is to a good approximation a plane standing wave, propagating along the $\pm z$ directions. For this reason, we neglect the longitudinal, i.e., $\mathbf{e}_0 = \hat{\mathbf{z}}$, component of the field. The relevant portion of α_{ij}, in Cartesian components $(\hat{\mathbf{x}}, \hat{\mathbf{y}})$, is then

$$\alpha_{ij} = \alpha_0\left[\frac{1}{2}\begin{pmatrix}1 & 0\\ 0 & 1\end{pmatrix} + \frac{2(-1)^{J-1/2}S_z}{[J]}\begin{pmatrix}0 & i\\ -i & 0\end{pmatrix}\right], \tag{A6}$$

which has eigenvectors $\mathbf{e}_\pm$, corresponding to $\sigma_\pm$ polarizations. For the D_1 ($J = 1/2$) and D_2 ($J = 3/2$) transitions, the corresponding eigenvalues are

$$\alpha_\pm^{D_1} = \alpha_0\left(\tfrac{1}{2} \mp S_z\right), \tag{A7}$$

$$\alpha_\pm^{D_2} = \alpha_0\left(\tfrac{1}{2} \pm \tfrac{1}{2}S_z\right). \tag{A8}$$

From this we see that other components of $\mathbf{S}$ do not contribute to the polarizability.

Using Eq. (A1), $\sigma_\pm$ light on the D_2 and D_1 transitions experiences

$$n_\pm^{D_1} - 1 \approx \frac{\pi n_{\rm A} r_e c^2 f_{\rm osc}^{D_1}}{\omega_{\rm at}^{D_1}} \frac{-1}{\Delta + i\Gamma_2}(1 \mp 2S_z), \tag{A9}$$

$$n_\pm^{D_2} - 1 \approx \frac{\pi n_{\rm A} r_e c^2 f_{\rm osc}^{D_2}}{\omega_{\rm at}^{D_2}} \frac{-1}{\Delta + i\Gamma_2}(1 \pm S_z), \tag{A10}$$

where $f_{\rm osc}^{D_1} \approx 0.3423$ and $f_{\rm osc}^{D_2} \approx 0.6958$ are the transition oscillator strengths.

APPENDIX B: SPIN-DEPENDENT MEDIUM REFRACTIVE INDEX

As described in Appendix A, in conditions relevant to many miniaturized sensors, i.e., realistic vapor density, high buffer gas pressure, and optical powers that do not saturate the optical transition [58], the refractive index for light near the D_1 or D_2 transition with $\sigma_\pm$ circular polarization (quantization axis is along z) is

$$n_\pm - 1 \approx \frac{\pi n_{\rm A} r_e c^2 f_{\rm osc}}{\omega_{\rm at}} \frac{-1}{\Delta + i\Gamma_2}(1 \pm \tilde{\alpha}^{(1)}S_z), \tag{B1}$$

where n_A is the atomic number density, r_e is the classical electron radius, c is the speed of light, $f_{\rm osc}$ is the transition oscillator strength ($f_{\rm osc}^{D_1} \approx 0.3423$ and $f_{\rm osc}^{D_2} \approx 0.6958$ in ^{87}Rb), $\omega_{\rm at}$ is the transition angular frequency, $\Delta \equiv \omega - \omega_{\rm at}$ is the detuning, ω is the optical angular frequency, Γ_2 is the transverse relaxation rate of the optical transition, and thus the (angular frequency) half width at half maximum of the collisionally broadened absorption spectrum, $\tilde{\alpha}^{(1)} = -2$ for the D_1 transition or $\tilde{\alpha}^{(1)} = 1$ for the D_2 transition, and S_z is the on-axis spin polarization. For brevity, we define $n' \equiv {\rm Re}[n]$ and $n'' \equiv {\rm Im}[n]$.

Upon passing through a cell of length $L_{\rm at}$, the transmission amplitude attributable to the atoms (as opposed to the distance traveled or atom-independent losses) is

$$t_A = \exp\left[i\frac{(n-1)\omega}{c}L_{\rm at}\right]. \tag{B2}$$

We note that n is linear in S_z, that the real and imaginary parts of $(n-1)$ are affected by S_z in the same proportion, and that, for both D_1 and D_2, the sign of dn/dS_z reverses with a change in circular polarization. The on-resonance optical depth of the unpolarized medium is

$$\mathcal{D}_0 = \frac{n''\omega_{\rm at}L_{\rm at}}{c} = \frac{\pi n_{\rm A} r_e c f_{\rm osc} L_{\rm at}}{\Gamma_2}, \tag{B3}$$

and it is convenient to write Eq. (B2) as

$$t_{\rm A} = \exp\left[i\frac{-\Gamma_2}{\Delta + i\Gamma_2}(1 \pm \tilde{\alpha}^{(1)}S_z)\mathcal{D}_0\right]. \tag{B4}$$

APPENDIX C: CAVITY TRANSMISSION, REFLECTION, AND ABSORPTION

The cavity is formed by mirrors M_i, $i \in \{1, 2\}$, with 1 being the mirror via which laser power enters, and 2 being the other mirror, with amplitude transmission and reflection coefficients t_i and r_i, respectively. We adopt the convention that all mirror reflection and transmission coefficients are positive real, with the exception of reflection of a beam approaching from outside the cavity, in which case the reflection amplitude is negative real. We assume lossless mirrors, and thus $r_i^2 + t_i^2 = 1$ (equivalent losses will be incorporated elsewhere in the model). The cavity contains a vapor cell of interior length $L_{\rm at}$ and single-pass transmission amplitude $t_{\rm cell} = t_{\rm win}^2 t_{\rm A} \exp[iL_{\rm at}\omega/c]$, where $t_{\rm A}$, defined in Eq. (B2), is the atomic contribution and $t_{\rm win}$ is the amplitude transmission of a single-cell window. Because of scattering losses, $|t_{\rm win}|^2$ may be less than unity.

The optical path length between the mirrors, not including the atomic contribution to n, is $L_{\rm cav}$, so, for an empty cell, or in the limit of large detuning from atomic resonance, the FSR (a linear frequency) is $\Delta\nu_{\rm FSR} \equiv c/2L_{\rm cav}$.

The frequency-dependent cavity transmission amplitude can be calculated by summing the transmission amplitude for all trajectories [45] as

$$\begin{aligned} t_{\rm cav} &= t_1 t_{\rm cell} t_2 \exp\left[i\frac{(L_{\rm cav}-L_{\rm at})\omega}{c}\right] \\ &\quad\times \sum_{n=0}^{\infty}\left(r_2 r_1 t_{\rm cell}^2 \exp\left[i\frac{2(L_{\rm cav}-L_{\rm at})\omega}{c}\right]\right)^n \\ &= \frac{t_1 t_2 |t_{\rm win}^2| t_{\rm A} \exp[i(\omega/\Delta\nu_{\rm FSR}+\Phi)/2]}{1-r_1 r_2 |t_{\rm win}^4| t_{\rm A}^2 \exp[i(\omega/\Delta\nu_{\rm FSR}+\Phi)]}, \end{aligned} \tag{C1}$$

where $\Phi \equiv \arg(t_{\rm win}^4)$. The cavity transmission probability is thus

$$|t_{\rm cav}|^2 = \left|\frac{t_1 t_2 t_{\rm win}^2 t_{\rm A}}{1-r_1 r_2 |t_{\rm win}^4| t_{\rm A}^2 \exp[i(\omega/\Delta\nu_{\rm FSR}+\Phi)]}\right|^2. \tag{C2}$$

In calculating the above we have neglected etalon effects from reflections from the interfaces of the cell windows [59]. The etalon effects can explain the asymmetry that is observed in the experimentally measured transmission peaks shown in Fig. 2.

The reflection amplitude is computed in the same way, and is given by

$$\begin{aligned} r_{\rm cav} &= -r_1 + t_1^2 r_2 t_{\rm cell}^2 \exp\left[i\frac{2(L_{\rm cav}-L_{\rm at})\omega}{c}\right] \\ &\quad\times \sum_{n=0}^{\infty}\left(r_1 t_{\rm cell}^2 r_2 \exp\left[i\frac{2(L_{\rm cav}-L_{\rm at})\omega}{c}\right]\right)^n \\ &= \frac{-r_1 + r_2 |t_{\rm win}^4| t_{\rm A}^2 \exp[i(\omega/\Delta\nu_{\rm FSR}+\Phi)]}{1-r_1 r_2 |t_{\rm win}^4| t_{\rm A}^2 \exp[i(\omega/\Delta\nu_{\rm FSR}+\Phi)]}. \end{aligned} \tag{C3}$$

Resonance occurs when $\mathrm{mod}_{2\pi}(2\arg t_{\rm A} + \omega/\Delta\nu_{\rm FSR} + \Phi) = 0$. The cavity resonances have finesse $\mathcal{F} \approx \pi/(1-|r_1 r_2 t_{\rm win}^4 t_{\rm A}^2|)$ and FWHM linewidth $\Gamma_{\rm cav} \equiv \Delta\nu_{\rm FSR}/\mathcal{F}$, which will depend on detuning from the atomic resonance.

APPENDIX D: CAVITY RESONANCE SHIFTS DUE TO ATOMIC SPIN POLARIZATION

From Eqs. (B2), (C2), and (C3), we see that the dependencies of $r_{\rm cav}$ and $|t_{\rm cav}|^2$ on the probe frequency ω and spin polarization S_z, through the refractive index n, is contained in the factor

$$t_{\rm A}^2 \exp\left[i\left(\frac{\omega}{\Delta\nu_{\rm FSR}}+\Phi\right)\right] = \exp\left[-2\frac{n''\omega}{c}L_{\rm at}\right]\exp[i\phi(\omega)], \tag{D1}$$

where the net intracavity round-trip phase is

$$\phi(\omega) \equiv 2\frac{(n'-1)\omega}{c}L_{\rm at} + \frac{\omega}{\Delta\nu_{\rm FSR}} + \Phi. \tag{D2}$$

In terms of ϕ, the optical resonance defined after Eq. (C3) occurs when $\mathrm{mod}_{2\pi}\phi(\omega) = 0$. Maintaining resonance by holding ϕ constant, and using Eq. (B4),

$$\begin{aligned} \left(\frac{\partial\omega}{\partial S_z}\right)_\phi &= -\left(\frac{\partial\phi}{\partial\omega}\right)^{-1}\left(\frac{\partial\phi}{\partial S_z}\right) \\ &= \frac{\pm\omega}{(n'-1)L_{\rm at}+L_{\rm cav}}\frac{\mathcal{D}_0 c\tilde{\alpha}^{(1)}}{\omega_{\rm at}}\frac{\Delta\Gamma_2}{\Delta^2+\Gamma_2^2} \\ &\approx \frac{\pm\omega}{L_{\rm cav}}\frac{\mathcal{D}_0 c\tilde{\alpha}^{(1)}}{\omega_{\rm at}}\frac{\Delta\Gamma_2}{\Delta^2+\Gamma_2^2}. \end{aligned} \tag{D3}$$

To express this in terms of linear frequency ν, we use $\delta\omega_{\rm res} = 2\pi\delta\nu_{\rm res}$, $\omega = 2\pi\nu$, $\omega_{\rm at} = 2\pi\nu_{\rm at}$, $\Delta = 2\pi(\nu-\nu_{\rm at})$, $\Gamma_2 = 2\pi\Delta\nu_{\rm opt}^{D_2}/2$, where $\Delta\nu_{\rm opt}^{D_2}$ is the FWHM of absorption in linear frequency. Making these substitutions, the shift in resonance frequency is given by

$$\delta\nu = \frac{\pm\mathcal{D}_0 c\tilde{\alpha}^{(1)}}{4\pi L_{\rm cav}}\frac{\nu}{\nu_{\rm at}}\frac{(\Delta\nu_{\rm opt}^{D_2}/2)(\nu-\nu_{\rm at})}{(\nu-\nu_{\rm at})^2+(\Delta\nu_{\rm opt}^{D_2}/2)^2}P_z, \tag{D4}$$

where we have defined the degree of polarization $P_z = 2S_z$ equal to 1 for maximum spin polarization [47,48].

APPENDIX E: PDH ERROR SIGNAL

Because of phase modulation with amplitude β, the amplitude of the probe field arriving to the cavity is

$$\begin{aligned} \mathcal{E}_{\rm in}(t) &= \sqrt{P_{\rm las}}e^{-i[\omega_0 t+\beta\sin(\Omega t)]} \\ &= \sqrt{P_{\rm las}}\sum_{k=-\infty}^{k=\infty} J_k(\beta)e^{-i\omega_k t}, \end{aligned} \tag{E1}$$

where $P_{\rm las}$ is the laser power, J_n is the Bessel function of the first kind and order n, $\omega_k \equiv \omega_0 + k\Omega$, and the second equality follows from the Jacobi-Anger expansion.

The light reflected from the cavity has amplitude

$$\mathcal{E}_{\rm ref}(t) = \sqrt{P_{\rm las}}\sum_{k=-\infty}^{\infty} r_{\rm cav}(\omega_k)J_k(\beta)e^{-i\omega_k t}, \tag{E2}$$

where $r_{\rm cav}(\omega)$ is the cavity reflection amplitude of Eq. (C3).

The mean power arriving to the photodetector is

$$\begin{aligned}\bar{P}_{\mathrm{ref}}(t) &= |\mathcal{E}_{\mathrm{ref}}(t)|^2 \\ &= P_{\mathrm{las}} \sum_{k=-\infty}^{\infty} \sum_{k'=-\infty}^{\infty} J_k(\beta) J_{k'}(\beta) r^*_{\mathrm{cav}}(\omega_k) r_{\mathrm{cav}}(\omega_{k'}) \\ &\quad \times e^{-i(\omega_{k'}-\omega_k)t}, \end{aligned} \tag{E3}$$

which has a dc component

$$\begin{aligned}\bar{P}_{\mathrm{ref},0}(t) &= P_{\mathrm{las}} \sum_{k=-\infty}^{\infty} r^*_{\mathrm{cav}}(\omega_k) J_k(\beta) e^{i\omega_k t} \\ &\quad \times \sum_{k'=-\infty}^{\infty} r_{\mathrm{cav}}(\omega_{k'}) J_{k'}(\beta) e^{-i\omega_{k'} t} \delta_{k',k} \\ &= P_{\mathrm{las}} \sum_{k=-\infty}^{\infty} |r_{\mathrm{cav}}(\omega_k) J_k(\beta)|^2 \end{aligned} \tag{E4}$$

and a component oscillating at frequency Ω,

$$\begin{aligned}\bar{P}_{\mathrm{ref},\Omega}(t) &= P_{\mathrm{las}} \sum_{k=-\infty}^{\infty} \sum_{k'=-\infty}^{\infty} r^*_{\mathrm{cav}}(\omega_k) J_k(\beta) e^{i\omega_k t} \\ &\quad \times r_{\mathrm{cav}}(\omega_{k'}) J_{k'}(\beta) e^{-i\omega_{k'} t} (\delta_{k',k+1} + \delta_{k'+1,k}) \\ &= P_{\mathrm{las}} \sum_{k=-\infty}^{\infty} J_k(\beta) J_{k+1}(\beta) \\ &\quad \times 2\mathrm{Re}[r^*_{\mathrm{cav}}(\omega_k) r_{\mathrm{cav}}(\omega_{k+1}) e^{-i\Omega t}]. \end{aligned} \tag{E5}$$

When demodulated with phase φ, and with system gain K, the resulting error signal is

$$\epsilon = K \sum_{k=-\infty}^{\infty} J_k(\beta) J_{k+1}(\beta) 2\mathrm{Re}[r^*_{\mathrm{cav}}(\omega_k) r_{\mathrm{cav}}(\omega_{k+1}) e^{i\varphi}]. \tag{E6}$$

[1] C. Cohen-Tannoudji and A. Kastler, Optical pumping, Prog. Opt. **5**, 1 (1966).

[2] W. Happer, Optical pumping, Rev. Mod. Phys. **44**, 169 (1972).

[3] W. Bell, A. Bloom, and R. Williams, A microwave frequency standard employing optically pumped sodium vapor, IRE Trans. Microwave Theory Tech. **7**, 95 (1959).

[4] J. Dupont-Roc, S. Haroche, and C. Cohen-Tannoudji, Detection of very weak magnetic fields (10^{-9} gauss) by ^{87}Rb zero-field level crossing resonances, Phys. Lett. A **28**, 638 (1969).

[5] T. W. Kornack, R. K. Ghosh, and M. V. Romalis, Nuclear spin gyroscope based on an atomic comagnetometer, Phys. Rev. Lett. **95**, 230801 (2005).

[6] T. G. Walker and M. S. Larsen, in *Advances In Atomic, Molecular, and Optical Physics*, Vol. 65, edited by E. Arimondo, C. C. Lin, and S. F. Yelin (Academic Press, Cambridge, 2016), pp. 373–401.

[7] M. S. Safronova, D. Budker, D. DeMille, D. F. J. Kimball, A. Derevianko, and C. W. Clark, Search for new physics with atoms and molecules, Rev. Mod. Phys. **90**, 025008 (2018).

[8] R. H. Dicke, The effect of collisions upon the Doppler width of spectral lines, Phys. Rev. **89**, 472 (1953).

[9] M. A. Bouchiat and J. Brossel, Relaxation of optically pumped Rb atoms on paraffin-coated walls, Phys. Rev. **147**, 41 (1966).

[10] S. Karlen, J. Gobet, T. Overstolz, J. Haesler, and S. Lecomte, Lifetime assessment of RbN_3-filled MEMS atomic vapor cells with Al_2O_3 coating, Opt. Express **25**, 2187 (2017).

[11] J. Kitching, Chip-scale atomic devices, Appl. Phys. Rev. **5**, 031302 (2018).

[12] S. Dyer, K. Gallacher, U. Hawley, A. Bregazzi, P. Griffin, A. Arnold, D. Paul, E. Riis, and J. McGilligan, Chip-scale packages for a tunable wavelength reference and laser cooling platform, Phys. Rev. Appl. **19**, 044015 (2023).

[13] V. G. Lucivero, A. Zanoni, G. Corrielli, R. Osellame, and M. W. Mitchell, Laser-written vapor cells for chip-scale atomic sensing and spectroscopy, Opt. Express **30**, 27149 (2022).

[14] W. C. Griffith, S. Knappe, and J. Kitching, Femtotesla atomic magnetometry in a microfabricated vapor cell, Opt. Express **18**, 27167 (2010).

[15] R. Cipolletti, J. Riedrich-Moeller, T. Fuchs, A. Wickenbrock, and D. Budker, in *2021 IEEE Sensors* (IEEE, Sydney, 2021), pp. 1–4.

[16] R. Jiménez-Martínez and S. Knappe, in *High Sensitivity Magnetometers*, edited by A. Grosz, M. J. Haji-Sheikh, and S. C. Mukhopadhyay (Springer International Publishing, Cham, 2017), pp. 523–551.

[17] M. T. Hummon, S. Kang, D. G. Bopp, Q. Li, D. A. Westly, S. Kim, C. Fredrick, S. A. Diddams, K. Srinivasan, V. Aksyuk, and J. E. Kitching, Photonic chip for laser stabilization to an atomic vapor with 10^{-11} instability, Optica **5**, 443 (2018).

[18] D. Hunter, C. Perrella, A. McWilliam, J. P. McGilligan, M. Mrozowski, S. J. Ingleby, P. F. Griffin, D. Burt, A. N. Luiten, and E. Riis, Free-induction-decay magnetic field imaging with a microfabricated Cs vapor cell, Opt. Express **31**, 33582 (2023).

[19] C. Troullinou, R. Jiménez-Martínez, J. Kong, V. G. Lucivero, and M. W. Mitchell, Squeezed-light enhancement and backaction evasion in a high sensitivity optically pumped magnetometer, Phys. Rev. Lett. **127**, 193601 (2021).

[20] C. Troullinou, V. G. Lucivero, and M. W. Mitchell, Quantum-enhanced magnetometry at optimal number density, Phys. Rev. Lett. **131**, 133602 (2023).

[21] V. Lucivero, W. Lee, N. Dural, and M. Romalis, Femtotesla direct magnetic gradiometer using a single multipass cell, Phys. Rev. Appl. **15**, 014004 (2021).

[22] R. J. Cooper, D. W. Prescott, P. Matz, K. L. Sauer, N. Dural, M. V. Romalis, E. L. Foley, T. W. Kornack, M. Monti, and J. Okamitsu, Atomic magnetometer multisensor array for rf

interference mitigation and unshielded detection of nuclear quadrupole resonance, Phys. Rev. Appl. **6**, 064014 (2016).
[23] M. Limes, E. Foley, T. Kornack, S. Caliga, S. McBride, A. Braun, W. Lee, V. Lucivero, and M. Romalis, Portable magnetometry for detection of biomagnetism in ambient environments, Phys. Rev. Appl. **14**, 011002 (2020).
[24] D. Sheng, S. Li, N. Dural, and M. V. Romalis, Subfemtotesla scalar atomic magnetometry using multipass cells, Phys. Rev. Lett. **110**, 160802 (2013).
[25] S. Li, P. Vachaspati, D. Sheng, N. Dural, and M. V. Romalis, Optical rotation in excess of 100 rad generated by Rb vapor in a multipass cell, Phys. Rev. A **84**, 061403 (2011).
[26] B. Q. Baragiola, L. M. Norris, E. Montaño, P. G. Mickelson, P. S. Jessen, and I. H. Deutsch, Three-dimensional light-matter interface for collective spin squeezing in atomic ensembles, Phys. Rev. A **89**, 033850 (2014).
[27] D. Hunger, T. Steinmetz, Y. Colombe, C. Deutsch, T. W. Hänsch, and J. Reichel, A fiber Fabry–Perot cavity with high finesse, New J. Phys. **12**, 065038 (2010).
[28] E. M. Purcell, in *Proceedings of the American Physical Society*, Vol. 69 (American Physical Society, New York, 1946), p. 681.
[29] J. Lodewyck, P. G. Westergaard, and P. Lemonde, Nondestructive measurement of the transition probability in a Sr optical lattice clock, Phys. Rev. A **79**, 061401 (2009).
[30] M. Abgrall, B. Chupin, L. De Sarlo, J. Guéna, P. Laurent, Y. Le Coq, R. Le Targat, J. Lodewyck, M. Lours, P. Rosenbusch, G. D. Rovera, and S. Bize, Atomic fountains and optical clocks at SYRTE: Status and perspectives, *The measurement of time / La mesure du temps*, C. R. Phys. **16**, 461 (2015).
[31] J. G. Bohnet, K. C. Cox, M. A. Norcia, J. M. Weiner, Z. Chen, and J. K. Thompson, Reduced spin measurement back-action for a phase sensitivity ten times beyond the standard quantum limit, Nat. Photonics **8**, 731 (2014).
[32] O. Hosten, N. J. Engelsen, R. Krishnakumar, and M. A. Kasevich, Measurement noise 100 times lower than the quantum-projection limit using entangled atoms, Nature **529**, 505 (2016).
[33] K. C. Cox, G. P. Greve, J. M. Weiner, and J. K. Thompson, Deterministic squeezed states with collective measurements and feedback, Phys. Rev. Lett. **116**, 093602 (2016).
[34] C. Mazzinghi, D. B. Orenes, P. Gomez, V. G. Lucivero, E. Aybar, S. Gugnani, and M. W. Mitchell, Cavity-enhanced polarization rotation measurements for low-disturbance probing of atoms, Opt. Express **29**, 40854 (2021).
[35] H. Crepaz, L. Y. Ley, and R. Dumke, Cavity enhanced atomic magnetometry, Sci. Rep. **5**, 15448 (2015).
[36] G. Vasilakis, H. Shen, K. Jensen, M. Balabas, D. Salart, B. Chen, and E. S. Polzik, Generation of a squeezed state of an oscillator by stroboscopic back-action-evading measurement, Nat. Phys. **11**, 389 (2015).
[37] G. Chatzidrosos, A. Wickenbrock, L. Bougas, N. Leefer, T. Wu, K. Jensen, Y. Dumeige, and D. Budker, Miniature cavity-enhanced diamond magnetometer, Phys. Rev. Appl. **8**, 044019 (2017).
[38] K. Sycz, W. Gawlik, and J. Zachorowski, Resonant Faraday effect in a Fabry–Perot cavity, Opt. Appl. **40**, 633 (2010).
[39] H. Y. Ling, Theoretical investigation of transmission through a Faraday-active Fabry–Perot étalon, J. Opt. Soc. Am. A **11**, 754 (1994).
[40] R. V. Pound, Electronic frequency stabilization of microwave oscillators, Rev. Sci. Instrum. **17**, 490 (2004).
[41] R. W. P. Drever, J. L. Hall, F. V. Kowalski, J. Hough, G. M. Ford, A. J. Munley, and H. Ward, Laser phase and frequency stabilization using an optical resonator, Appl. Phys. B **31**, 97 (1983).
[42] E. D. Black, An introduction to Pound–Drever–Hall laser frequency stabilization, Am. J. Phys. **69**, 79 (2001).
[43] G. C. Bjorklund, M. D. Levenson, W. Lenth, and C. Ortiz, Frequency modulation (FM) spectroscopy, Appl. Phys. B **32**, 145 (1983).
[44] W. Happer, Y. Y. Jau, and T. Walker, *Optically Pumped Atoms* (Wiley, Weinheim, 2010).
[45] M. Born, E. Wolf, and A. Bhatia, *Principles of Optics* (Cambridge University Press, Cambridge, 2019).
[46] M. V. Romalis, E. Miron, and G. D. Cates, Pressure broadening of Rb D_1 and D_2 lines by ^{3}He, ^{4}He, N_2, and Xe: Line cores and near wings, Phys. Rev. A **56**, 4569 (1997).
[47] S. J. Seltzer, Ph.D. thesis, Princeton University, 2008.
[48] V. Shah and M. V. Romalis, Spin-exchange relaxation-free magnetometry using elliptically polarized light, Phys. Rev. A **80**, 013416 (2009).
[49] J. Kong, V. G. Lucivero, R. Jimé nez-Martínez, and M. W. Mitchell, Long-term laser frequency stabilization using fiber interferometers, Rev. Sci. Instrum. **86**, 073104 (2015).
[50] Y. Ito, D. Sato, K. Kamada, and T. Kobayashi, Optimal densities of alkali metal atoms in an optically pumped K-Rb hybrid atomic magnetometer considering the spatial distribution of spin polarization, Opt. Express **24**, 15391 (2016).
[51] N. Mizutani, K. Okano, K. Ban, S. Ichihara, A. Terao, and T. Kobayashi, A plateau in the sensitivity of a compact optically pumped atomic magnetometer, AIP Adv. **4**, 057132 (2014).
[52] K. Mouloudakis, G. Vasilakis, V. G. Lucivero, J. Kong, I. K. Kominis, and M. W. Mitchell, Effects of spin-exchange collisions on the fluctuation spectra of hot alkali-metal vapors, Phys. Rev. A **106**, 023112 (2022).
[53] D. Das and A. C. Wilson, Very long optical path-length from a compact multi-pass cell, Appl. Phys. B **103**, 749 (2011).
[54] J. F. Tasker, J. Frazer, G. Ferranti, E. J. Allen, L. F. Brunel, S. Tanzilli, V. D'Auria, and J. C. F. Matthews, Silicon photonics interfaced with integrated electronics for 9 GHz measurement of squeezed light, Nat. Photonics **15**, 11 (2021).
[55] S. Lischke, D. Knoll, C. Mai, L. Zimmermann, A. Peczek, M. Kroh, A. Trusch, E. Krune, K. Voigt, and A. Mai, High bandwidth, high responsivity waveguide-coupled germanium p-i-n photodiode, Opt. Express **23**, 27213 (2015).
[56] A. Yariv, *Quantum Electronics* (Wiley, Hoboken (NJ), 1989).
[57] W. Happer and B. S. Mathur, Effective operator formalism in optical pumping, Phys. Rev. **163**, 12 (1967).
[58] The model does apply for optical powers that saturate optical pumping.
[59] These amplitudes are in practice much smaller than the near-unity reflection amplitude of the cavity mirrors, and can be made still smaller through antireflection coating. Their inclusion significantly complicates the resulting expressions without qualitatively changing the results.